

Objective Maps of Near-Surface Flow States near Point Conception, California

E. P. DEVER

Integrative Oceanography Division, Scripps Institution of Oceanography, University of California, San Diego, La Jolla, California

(Manuscript received 4 November 2002, in final form 25 July 2003)

ABSTRACT

Objective streamfunction and velocity potential maps of three commonly observed flow states near Point Conception, California, are derived from moored current-meter and drifter observations. The states are defined using current-meter data. Drifter data are sorted by flow state and averaged within spatial bins to resolve their spatial structures. Spatial correlations of drifter data show the along-shelf and cross-shelf decorrelation distances are approximately 45 and 25 km, respectively. This information is used to make the objective streamfunction and velocity potential maps. The total velocity is represented as the sum of the rotational, nondivergent streamfunction component and the irrotational, divergent velocity potential component. The velocity derived from the streamfunction is much stronger than that derived from the velocity potential. The streamfunction is sufficiently well resolved to make meaningful vorticity maps. The velocity potential indicates a source term in the western Santa Barbara Channel consistent with wind stress curl-driven upwelling, but divergence maps derived from the velocity potential are very noisy, making comparisons with wind stress curl mapped on the same scales problematic.

1. Introduction

Point Conception (Fig. 1) marks the transition between the relatively warm waters of the Southern California Bight and the cooler waters of the central California coast (Hendershott and Winant 1996). Seasonal salinity gradients also occur here. In spring, local upwelling near Point Conception causes high surface salinities there. In other seasons, the highest regional surface salinities are in the southern California Bight (Bray et al. 1999). The Santa Maria Basin (SMB), the southernmost portion of the central California shelf and slope, extends north from Point Conception to Point Buchon, about 100 km. Its shelf width is approximately 40 km. The Santa Barbara Channel (SBC), the northern limit of the Southern California Bight, is about 100 km in length from Point Conception to Port Hueneme. Four islands define its southern, offshore boundary. The western entrance to the channel is approximately 40 km wide with a sill depth of about 450 m. In the western channel, there is a deep basin of about 600-m depth and 50 km wide. The eastern entrance to the channel is relatively constricted with a width of 20 km and a maximum sill depth of 200 m.

The abrupt change in coastline orientation at Point Conception causes a large-scale difference in the wind

field between the central California coast and the Southern California Bight (Dorman and Winant 2000). Strong equatorward wind forcing often occurs in the SMB and at the western entrance to the SBC. The wind stress is predominantly along-shelf with an onshore component in the SMB and is diagonal across the channel in the western SBC. The eastern SBC is relatively sheltered and the wind forcing is weaker. Spatial variations in the wind field can force regional circulation by a number of mechanisms. On the scale of the Santa Barbara Channel, wind variations can cause spatial variability in the surface Ekman transport. Ekman transport divergence, in turn, is one mechanism of upwelling and has been speculated to cause some of the regional circulation features (Münchow 2000). Wind variations on the scale of the Southern California Bight can also affect the local circulation by inducing regional sea surface pressure gradients (Oey 1999; McCreary et al. 1987) and through remote forcing (Auad and Hendershott 1997).

In the SMB, where strong local wind forcing occurs, the near surface velocity is strongly coherent with the wind (Hendershott 2000) and the near-surface flow is generally equatorward in spring and summer (Winant et al. 2003). Below the surface, there is a tendency for poleward flow that is reversed only in spring (Strub et al. 1987). The subsurface poleward flow becomes progressively stronger in summer and reaches the surface in autumn before weakening in late winter.

At Point Conception, local atmospheric boundary layer dynamics (Rogerson 1999) intensify the wind. The wind forcing and local bathymetry combine to make

Corresponding author address: Dr. Edward P. Dever, Integrative Oceanography Division, 0209, Scripps Institution of Oceanography, University of California, San Diego, 9500 Gilman Drive, La Jolla, CA 92093-0209.
E-mail: edever@ucsd.edu

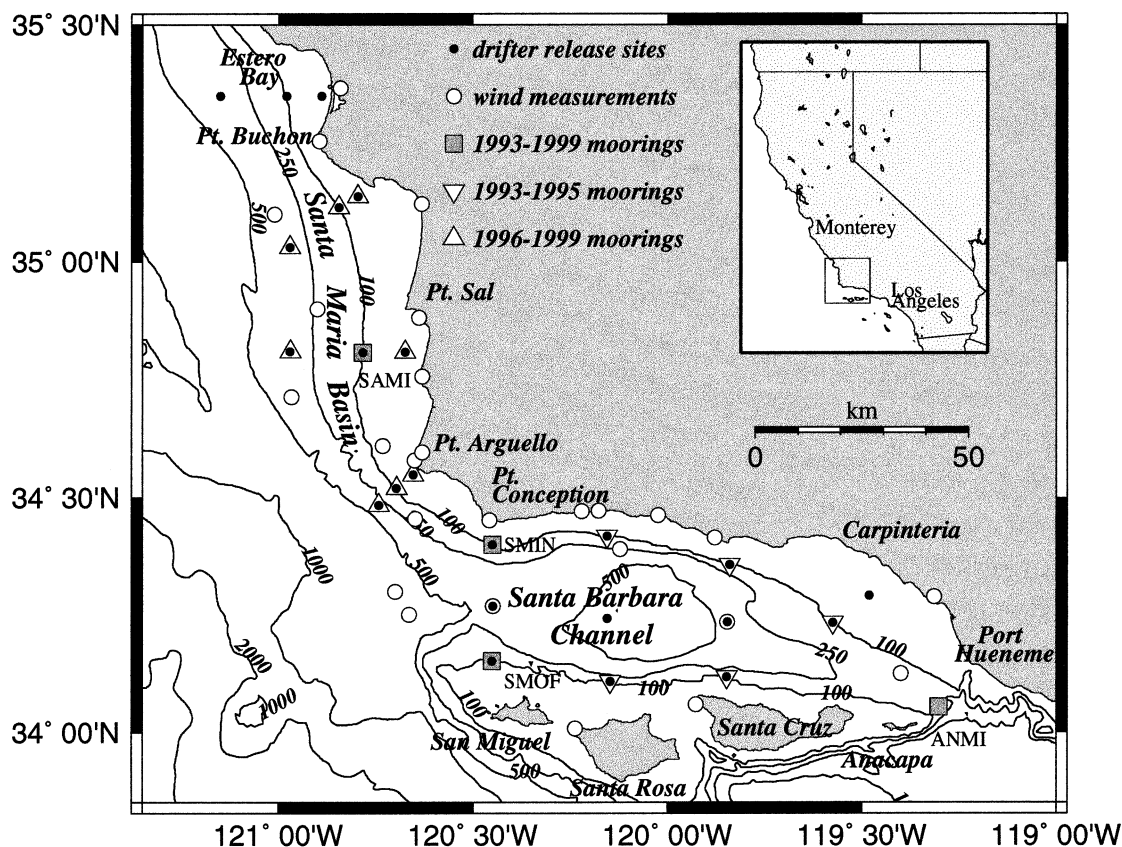


FIG. 1. The Santa Barbara Channel and Santa Maria Basin. From 1993 to 1995, drifters were released in the Santa Barbara Channel, with a single drifter released at the Santa Maria Basin 1993–99 mooring. From 1996 to 1999, drifters were released within the Santa Maria Basin and along the westernmost drifter line in the Santa Barbara Channel. About one-half of the 1996–99 drifter releases also included the other Santa Barbara Channel drifter release locations. Wind measurements include National Data Buoy Center (NDBC) buoy and coastal locations, instruments deployed on the shore and on oil platforms as part of this study, and other records obtained from private and local government agencies.

Point Conception the southernmost center of strong upwelling on the California coast. Upwelling commonly occurs in all seasons except late autumn and winter. Barth and Brink (1987) deduced upwelling pathways from ship acoustic Doppler current profile (ADCP), mooring, and surface drifter data and found them to be highly three-dimensional. Plumes resulting from upwelling can leave Point Conception by a variety of southward-trending paths (Atkinson et al. 1986). They can lead into the channel or may head southwest and pass outside San Miguel Island. In winter, when wind forcing is more variable, poleward flow generally occurs past Point Conception. The strongest poleward flow may leave the coast there and continue along the continental slope. Dever and Winant (2002) show a particularly clear example of poleward flow separation at Point Conception in November 1997 during the 1997–98 El Niño event.

Farther east, the circulation in the Santa Barbara Channel is not correlated in a simple way to wind forcing (Brink and Muench 1986). Instead, Harms and Winant (1998) suggested the SBC circulation pattern was

determined by a complex interplay between regional wind forcing and the generally poleward pressure gradient. They found strong upwelling favorable winds (0.1–0.5 Pa) in the absence of a strong poleward pressure gradient produced a three-dimensional upwelling state with upwelling near Point Conception and eastward flow along the channel islands to the eastern entrance of the SBC. As the poleward pressure gradient increased, upwelling continued at Point Conception but was now accompanied by westward flow at the eastern entrance to the channel and strong cyclonic recirculation in the western SBC. With weak upwelling winds and a strong pressure gradient, a strong poleward flow developed along the mainland coast of the SBC and past Point Conception. The variability of winds and pressure gradients over a range of time scales determined seasonal as well as synoptic variability. Seasonal patterns showed upwelling prevailed in spring, a strong cyclonic recirculation in summer, and poleward flow in autumn. Both winds and pressure gradient tended to be weakest in winter. Under each of these conditions a cyclonic circulation was present in the western SBC. During up-

welling the southern limb of the recirculation was strengthened, and during poleward flow its northern limb was strengthened.

The along-shelf wind-forced fluctuations in the SMB, the three-dimensional upwelling at Point Conception, and Santa Barbara Channel circulation patterns can be thought of as parts of a regional response encompassing the SBC and SMB. Using drifter and moored data, Winant et al. (2003) identified flow states we called upwelling, surface convergence, and relaxation. The upwelling state is marked by near-surface equatorward flow in the SMB and eastward flow along the channel islands in the SBC. The surface convergent state is marked by weaker equatorward flow in the SMB that converges with westward flow along the mainland coast of the SBC to form a strong offshore jet at Point Conception. In the SBC, westward flow along the mainland coast is continuous from the eastern SBC entrance to the western SBC. Within the western SBC, there is a strong cyclonic recirculation. The relaxation state is marked by poleward flow at the eastern SBC that continues along the mainland coast and over the shelf and slope of the SMB. There continues to be a recirculation in the western SBC, but the southern limb of this recirculation is weaker. The persistence scales of these states are synoptic, lasting from several days to several weeks. However, they have different probabilities of occurrence throughout the year. The upwelling pattern is prevalent in spring, the surface convergent pattern prevails in summer, and the relaxation pattern is prevalent in autumn and winter.

The goals of this paper are to objectively map, examine, and interpret the spatial structure of the near-surface circulation during these identified flow states. Drifter and moored near-surface currents will be used to map average synoptic states with a streamfunction and velocity potential representation. Vorticity estimates derived from the streamfunction will be examined in light of observed wind stress and predictions of previous model and observational studies. Divergence patterns will be estimated from the velocity potential and compared with those derived from wind stress curl.

The observations and data treatment, and spatial averaging procedures are described in section 2. The objective mapping procedures, mapped streamfunctions, and velocity potentials are described in section 3. Quantities derived from the objective maps and the limits of the mapping procedure are discussed in section 4. Conclusions are presented in section 5.

2. Observations

Our drifter data come from 29 deployments between May 1993 and November 1999 (Table 1). From 1993 to 1995, most drifters were released in the SBC with one drifter often released in the SMB. From 1996 to 1999, about one-half of drifter releases were at all locations shown in Fig. 1, while the other half were in

TABLE 1. Drifter release dates and description.

Release date	No. of drifters	Release positions
11 May 1993	12	SBC
26 Jul 1993	15	SBC
6 Oct 1993	11	SBC
8 Dec 1993	14	SBC
15 Feb 1994	12	SBC
13 Apr 1994	12	SBC
15 Jun 1994	13	SBC
13 Sep 1994	14	SBC
1 Nov 1994	11	SBC
31 Jan 1995	10	SBC
16 Mar 1995	11	SBC
16 May 1995	12	SBC
7 Jul 1995	11	SBC
24 Aug 1995	10	SBC
31 Oct 1995	12	SBC
10 Jan 1996	14	SMB
1 May 1996	11	SMB
3 Aug 1996	10	SMB
13 Sep 1996	9	SMB
17 Dec 1996	11	SMB
21 Mar 1997	28	SBC and SMB
20 Jul 1997	26	SBC and SMB
8 Nov 1997	24	SBC and SMB
17 Apr 1998	15	SMB
1 Jul 1998	25	SBC and SMB
27 Oct 1998	22	SBC and SMB
10 Mar 1999	22	SBC and SMB
3 Sep 1999	15	SMB
11 Nov 1999	25	SBC and SMB

the SMB and western SBC only. Additional data from a few drifters deployed in testing and for oil spill response drills are also used. To sample the seasonal variability, deployments were spaced about every 3–4 months. The drifter deployment positions were spaced approximately uniformly within the channel and basin (Fig. 1). Generally, one drifter was released at each location, although drifter pairs were occasionally released. Analysis of regional moored observations (Harms and Winant 1998) has shown that large-scale variability of the surface circulation pattern can often persist for a week or more. Because drifters usually exit the region or beach within 10 days, each drifter deployment generally samples one circulation pattern.

The surface drifters used are similar to the Davis (1985) Coastal Ocean Dynamics Experiment (CODE) design. The nominal sampling depth of the drifters is 0.5 m. Argos tracking was used to acquire positions for 40 days. Generally, four–five fixes per day are available with an accuracy of under 1 km (most often, under 300 m). Further information about the drifter sampling program, including example drifter trajectories, is found in Dever et al. (1998) and Winant et al. (1999, 2003).

Current-meter data come from moorings maintained between 1993 and 1999 in the SBC and SMB (Fig. 1). From 1993 to 1995, eight moorings were continuously maintained in the SBC and one (later two) moorings were maintained in the SMB. From 1996 to 1999, nine moorings were maintained in the SMB with three moor-

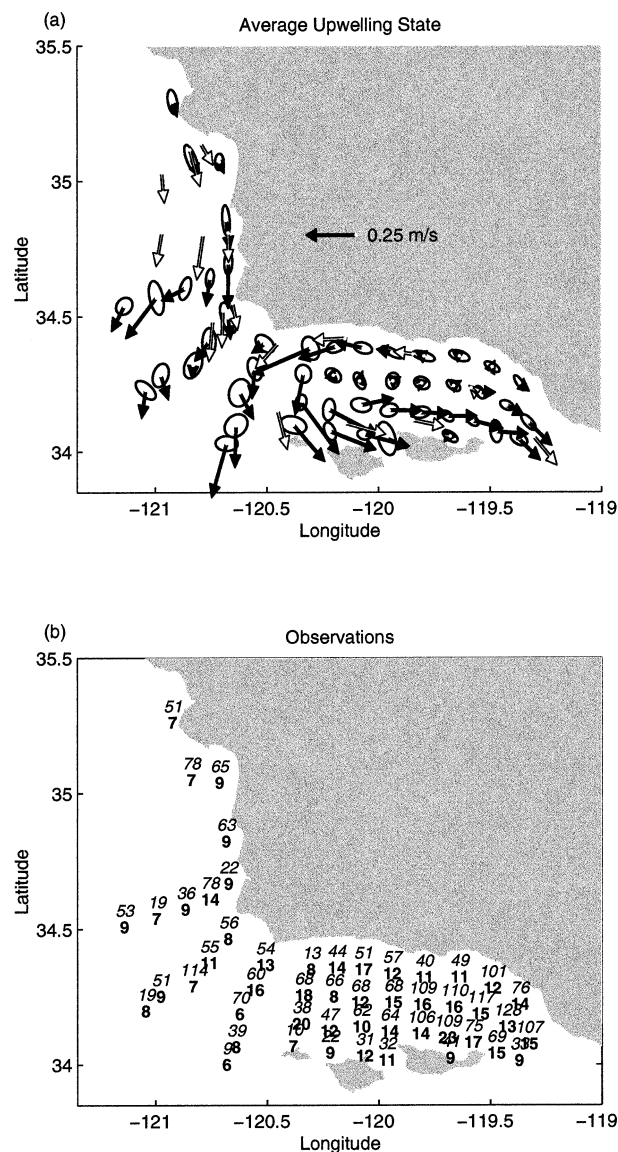


FIG. 2. (a) Upwelling means and standard errors along principal axes for moored (open arrows) and drifter velocities (solid arrows). (b) Total (top) and independent (bottom) number of drifter observations within each bin. Standard errors for drifter velocities are derived using the independent number of observations shown in (b).

ings retained in the SBC. Each mooring included a vector-measuring current meter (VMCM) 5 m beneath the surface as well as a number of deeper sensors. Further information about the moored measurements can be found in Hendershott and Winant (1996), Harms and Winant (1998), and Winant et al. (2003).

a. Data processing

In order to maintain temporal and spatial resolution, drifter fixes are not low-pass filtered. Instead they are linearly interpolated onto a 6-h averaged time base. Drifter statistics presented in Figs. 2–4 thus include tidal

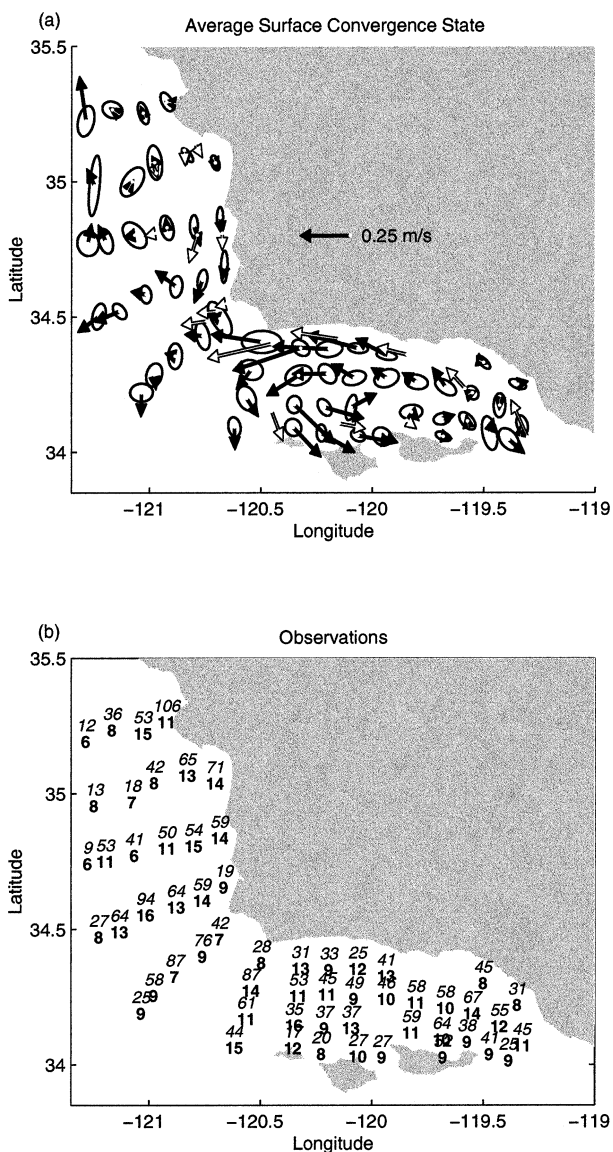


FIG. 3. As in Fig. 2 but for surface convergent means and standard errors.

and inertial variability. Drifter fixes within 1.5 km of the coast are removed because their behavior is quite different relative to fixes farther offshore and the uncertainty of the Argos position means it is possible they have beached. Velocities calculated from time differences of the interpolated positions are examined and any obviously unphysical velocities are then excluded from further analysis. To facilitate comparisons of drifter and current-meter statistics, VMCM data are also 6-h block-averaged onto the same time base. Further details regarding drifter data processing can be found in Dever et al. (1998).

Drifter velocity statistics are presented over approximately 12.5 km by 12.5 km bins in the SBC and 25 km (in the along-shelf direction) by 12.5 km (in the

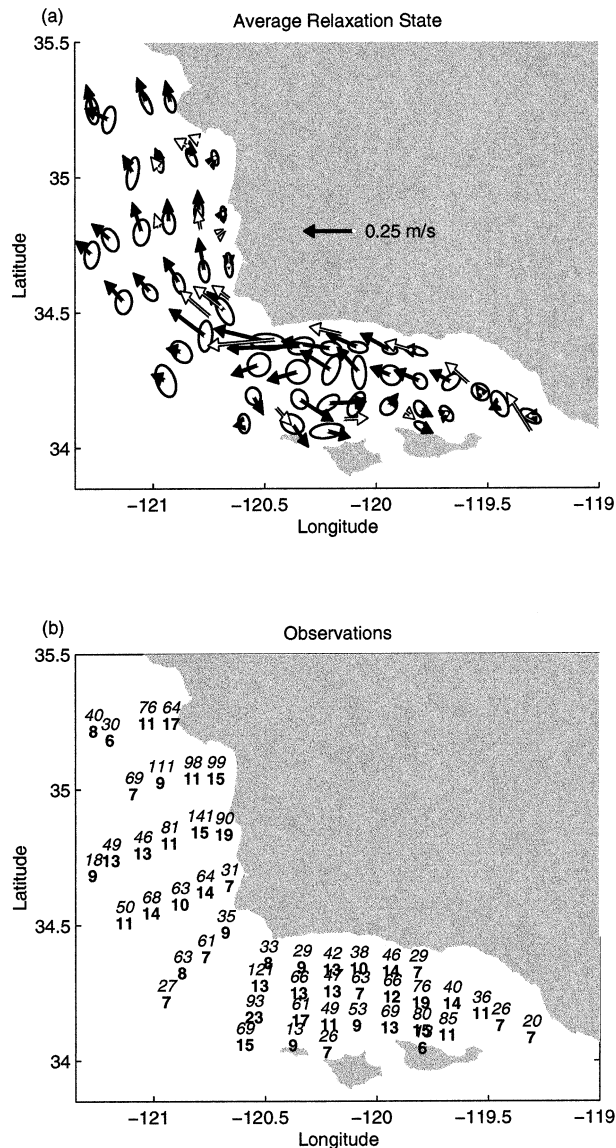


FIG. 4. As in Fig. 2 but for relaxation means and standard errors.

cross-shelf direction) bins in the SMB. The bin size is a compromise between the desires to maximize resolution and maintain statistical reliability. Drifter tracks and spatial correlations between moorings indicate these bin sizes are smaller than the appropriate spatial correlation scales and adequately resolve circulation features. Dever et al. (1998) derive a simplification of Davis (1991) expression for statistical uncertainty with the assumption that averaging areas are much smaller than the spatial scales, and that expression is used here to estimate statistical uncertainty of averages within spatial bins.

b. Averaging by synoptic states

Dever et al. (1998) presented overall mean and seasonal averages of drifter and current-meter data in the

Santa Barbara Channel. There the current-meter and drifter averages agreed well. Differences between the averages were consistent with near-surface shear estimates derived from a wind-driven log layer and from Stokes drift. However, when the same averaging procedures were applied to the Santa Maria Basin, disagreements between drifter and current-meter averages arose. Real near-surface shear, Stokes drift, statistical uncertainty, and the effects of small-scale diffusion on a nonuniform drifter sampling scheme (array bias; see e.g., Swenson and Niiler 1996) could not explain these differences. Instead, as is explained below, they are almost certainly caused by biases in drifter sampling of the large-scale states described in section 1.

Despite attempts to sample all ocean velocity and wind conditions, the upwelling state in the SMB was undersampled relative to the surface convergent and relaxation conditions. This occurred primarily for two reasons. The first reason was that the equatorward, offshore flow during upwelling (and to a lesser extent surface convergence) conditions led to a rapid exit of drifters deployed in the SMB. In contrast, relaxation conditions often led to drifters being retained in the SMB for longer times. Hence even, if drifter deployments sampled all states equally well, there would be fewer fixes under upwelling conditions. A related bias is the movement of drifters from the SBC into the SMB. This occurred only for relaxation conditions and further increased the bias of samples in the SMB toward relaxation. This is significant because deployments from 1993 to 1995 occurred in the SBC only, leading to biased sampling in the SMB for these deployments. A similar bias occurs at the eastern entrance to the SBC, where all deployments were made west of the averaging locations and drifter samples are biased toward upwelling conditions (Dever et al. 1998).

To minimize the drifter bias toward relaxation conditions, the moored data are used to identify the large-scale flow state (if one could be identified) and to average drifter velocities within spatial bins by flow state. Three of the four long-term moorings (Fig. 1) maintained from December 1993 and November 1999 are used to identify the flow state. Upwelling is defined to occur when the (subtidal) along-shelf flow in the Santa Maria Basin (SAMI) was southward and along-channel flow at the eastern entrance to the Santa Barbara Channel (ANMI) was southeastward (out of the channel). Surface convergence is defined to occur when along-shelf flow at SAMI was southward, along-channel flow at ANMI was northwestward (into the channel), and along-channel flow at Point Conception (SMIN) was westward. Relaxation is defined to occur when along-shelf flow at SAMI was northward, along-channel flow at ANMI was northwestward, and along-channel flow at SMIN was westward. Only days with good velocity data at each of ANMI, SMIN, and SAMI are considered to determine time series of which state, if any, exists. There is a roughly even breakdown of the different

states: 37% upwelling, 32% surface convergence, and 26% relaxation; 5% of the current-meter observations are not classifiable into one of these states.

1) AVERAGE UPWELLING STATE

The average upwelling state (Fig. 2) shows southward flow in the SMB past Point Arguello with eastward flow along the channel islands and out the eastern SBC entrance. Within the SMB, southward means are strongest between about the 75- and 350-m isobaths. Inshore, they are relatively weak. Offshore of the 350-m isobath, there are relatively few data points. The area between Point Arguello and Point Conception is generally considered to be the upwelling center (e.g., Barth and Brink 1987), and upwelling velocity averages here are quite interesting. Westward velocities from the SBC meet southward velocities from the SMB. Although the average velocities within this area are relatively weak, the variability as indicated by the standard deviation is high. South of Point Conception, in the western SBC and farther offshore, mean upwelling velocities are southward. There is an indication of flow bifurcation at San Miguel. West of San Miguel, velocity means are southward. North and east of San Miguel, they are southward and eastward, respectively. Eastward flow continues along the channel islands with a width of 25 km (two velocity bins). In contrast, westward mean velocities occur within 12.5 km of the mainland coast even during upwelling. Within the SBC, the mean upwelling flow resembles the spring mean calculated by Dever et al. (1998).

The number of data points used to calculate the upwelling means (Fig. 2) is far greater in the SBC than in the SMB. This happens for three reasons. More drifter releases occurred in the SBC than in the SMB, the SBC is downstream of the SMB for upwelling conditions, and drifters in the SBC tended to remain there longer because of some recirculation in the SBC as indicated by the means in Fig. 2a.

2) AVERAGE SURFACE CONVERGENT STATE

The average surface convergent state (Fig. 3) shows a strong cyclonic recirculation in the western SBC with a westward mean flow past Point Conception. A mean southward flow from the SMB combines with this westward flow at Point Arguello, hence the name surface convergent. The southward flow in the SMB is weaker than for the upwelling case, and it is confined to within 25 km of the coast. In the eastern SBC, the 5-m current-meter average is into the channel, but the surface drifter means are weak with a tendency for flow out of the channel. This disagreement is largely a consequence of biased drifter sampling in that the easternmost drifter sampling line ran from Santa Cruz Island to the mainland coast near Carpinteria. Drifter trajectories to the east of the line had a history of eastward flow, which

caused a bias in this direction. As Dever et al. (1998) point out, near-surface shear caused by wind or waves could also contribute to the eastward drifter means relative to the 5-m current meter at the eastern entrance of the SBC.

The spatial distribution of drifter data for the surface convergence state (Fig. 3b) is more even than that of the upwelling state. This is because drifter deployments captured more examples of the surface convergent state than of the upwelling state, and because drifters deployed in the SBC in the convergent state tended to head west past Point Conception, contributing to the drifter samples there.

3) AVERAGE RELAXATION STATE

The average relaxation state (Fig. 4) shows poleward flow from the eastern entrance of the Santa Barbara Channel, along the mainland coast past Points Conception and Arguello and into the Santa Maria Basin. Within the western Santa Barbara Channel there remains a cyclonic recirculation cell. As the poleward flow passes Point Conception the strongest flow leaves the coast and moves steadily offshore. As is the case for the convergent state, drifter means east of the easternmost drifter deployment line have means that do not agree in sign with the 5-m moored velocity means.

The spatial distribution of data for the relaxation state is fairly even. The areas with the lowest amounts of data are the eastern SBC and the area west and south of the SBC.

A comparison of the relative occurrence of synoptic patterns in the current-meter data, which are unbiased, with the drifter data shows that the drifter data are biased. For the current-meter data, there is a roughly even breakdown of the different states with a seasonal variation in the probability of different states occurring (Winant et al. 2003). Most common are upwelling in spring, surface convergence in summer, and relaxation in autumn. A comparison with the number of drifter observations for different synoptic states (Figs. 2b, 3b, 4b) shows there is a bias away from sampling upwelling. This bias is especially evident in the SMB. It has several causes. There is a tendency for drifters released during upwelling to be swept rapidly southward and offshore. Also drifters released in the SBC during surface convergent and relaxation conditions often enter the SMB, increasing the number of observations for these conditions. In the SBC, the bias is less evident. This may be a consequence of the cyclonic recirculation and the presence of the channel islands. These features help to equalize the residence time in the SBC for the different synoptic states.

3. Objective mapping of synoptic states

The bin-averaged velocities presented in section 2c indicate that the spatial structures of the synoptic states

are adequately resolved and that there is reasonable agreement between drifter and current-meter data. To learn more about the dynamics of these synoptic states, the bin-averaged drifter data together with the current-meter data are used to represent the near-surface velocity fields in terms of the objectively mapped streamfunction and velocity potential.

a. Method

Objective analysis (OA) has been widely used to map the velocity field in the atmosphere and ocean. Often the velocity has been mapped on a surface using a two-dimensional velocity streamfunction representation although the approach of mapping velocity components has also been used successfully (e.g., Carter and Robinson 1987). The streamfunction representation gives the rotational or nondivergent portion of the velocity field. Objective analysis can also be used to map the irrotational, divergent portion of the velocity field (Daley 1985) by representing the total velocity as the sum of rotational and divergent components using the Helmholtz theorem (Morse and Feshbach 1953). That is,

$$u = u_r + u_i = -\frac{d\psi}{dy} - \frac{d\chi}{dx} \quad \text{and} \\ v = v_r + v_i = \frac{d\psi}{dx} - \frac{d\chi}{dy},$$

where the subscripts r and i represent rotational and divergent (irrotational) velocity components, ψ and χ represent vector and scalar potentials, u is the cross-shelf velocity, v is the along-shelf velocity, x is the cross-shelf coordinate, and y is the along-shelf coordinate. In the literature of Daley (1985) and several other investigators, (e.g., Pedder 1989) ψ and χ are referred to as the streamfunction and velocity potential, and I will adopt their usage here.

Mapping the velocity as the sum of rotational and divergent components is much less common than mapping with the rotational component alone. This is because divergence estimates are prone to observational error. The divergent velocity is typically much weaker than the rotational velocity, and the two terms in the horizontal divergence often nearly cancel (Daley 1985). This is especially true in oceanography, for which data are scarcer and OA applications have often been to subsurface velocities for which quasigeostrophic, nondivergent dynamics are assumed to hold. However, for surface velocities in the coastal ocean, divergence has long been recognized to be critical to processes such as upwelling. Here the relatively rich dataset is used to map the total velocity as represented by the streamfunction and the velocity potential. Although the resulting velocity potentials remain noisy relative to the streamfunctions, the importance of obtaining even crude divergent velocity estimates in coastal upwelling regions makes the attempt worthwhile.

The OA methods used here closely follow those presented in Daley (1985) and Gille (2003), and I have adopted similar notation to help to clarify comparisons with their papers. Daley (1985) derives the covariance functions using a streamfunction and velocity potential representation with isotropic covariance functions. Gille (2003) derives OA streamfunctions using anisotropic correlation functions. I employ a streamfunction velocity potential representation of the velocity with anisotropic correlation functions under the assumptions that the streamfunction and velocity potential have identical spatial autocorrelations but that they are uncorrelated with each other. The velocity correlations can then be written

$$\langle u, u \rangle = \frac{1-\nu}{L_y^2} \left[-\left(1 - \frac{s^2}{L_y^2 \rho_o^2}\right) \frac{1}{\rho_o} \frac{dF}{d\rho_o} - \frac{s^2}{\rho_o^2 L_y^2} \frac{d^2 F}{d\rho_o^2} \right] \\ + \frac{\nu}{L_x^2} \left[-\left(1 - \frac{r^2}{L_x^2 \rho_o^2}\right) \frac{1}{\rho_o} \frac{dF}{d\rho_o} - \frac{r^2}{\rho_o^2 L_x^2} \frac{d^2 F}{d\rho_o^2} \right], \quad (1)$$

$$\langle v, v \rangle = \frac{1-\nu}{L_x^2} \left[-\left(1 - \frac{r^2}{L_x^2 \rho_o^2}\right) \frac{1}{\rho_o} \frac{dF}{d\rho_o} - \frac{r^2}{L_x^2 \rho_o^2} \frac{d^2 F}{d\rho_o^2} \right] \\ + \frac{\nu}{L_y^2} \left[-\left(1 - \frac{s^2}{L_y^2 \rho_o^2}\right) \frac{1}{\rho_o} \frac{dF}{d\rho_o} - \frac{s^2}{\rho_o^2 L_y^2} \frac{d^2 F}{d\rho_o^2} \right] \quad (2)$$

and

$$\langle u, v \rangle = \frac{(1-\nu)rs}{\rho_o^2 L_x^2 L_y^2} \left(-\frac{1}{\rho_o} \frac{dF}{d\rho_o} + \frac{d^2 F}{d\rho_o^2} \right) \\ - \frac{\nu rs}{\rho_o^2 L_x^2 L_y^2} \left(-\frac{1}{\rho_o} \frac{dF}{d\rho_o} + \frac{d^2 F}{d\rho_o^2} \right). \quad (3)$$

The ψ -velocity correlations are

$$\langle \psi, u \rangle = \frac{-(1-\nu)s}{L_y^2 \rho_o} \frac{dF}{d\rho_o} \quad \text{and} \\ \langle \psi, v \rangle = \frac{(1-\nu)r}{L_x^2 \rho_o} \frac{dF}{d\rho_o}, \quad (4)$$

and the χ -velocity correlations are

$$\langle \chi, u \rangle = \frac{\nu r}{L_x^2 \rho_o} \frac{dF}{d\rho_o} \quad \text{and} \quad \langle \chi, v \rangle = \frac{\nu s}{L_y^2 \rho_o} \frac{dF}{d\rho_o}, \quad (5)$$

where ν is the fractional variance in χ relative to the total variance in $\psi + \chi$, L_x and L_y are the cross-shelf and along-shelf correlation scales, F is the spatial correlation function for ψ and χ , ρ is the nondimensionalized scalar distance, r is the cross-shelf distance, and s is the along-shelf distance. The OA estimate of ψ is then

$$\psi = \mathbf{P}(\mathbf{A} + \varepsilon \mathbf{I})^{-1} \boldsymbol{\varphi}, \quad (6)$$

and the OA estimate of χ is

$$\chi = \mathbf{Q}(\mathbf{A} + \varepsilon \mathbf{I})^{-1} \boldsymbol{\varphi}, \quad (7)$$

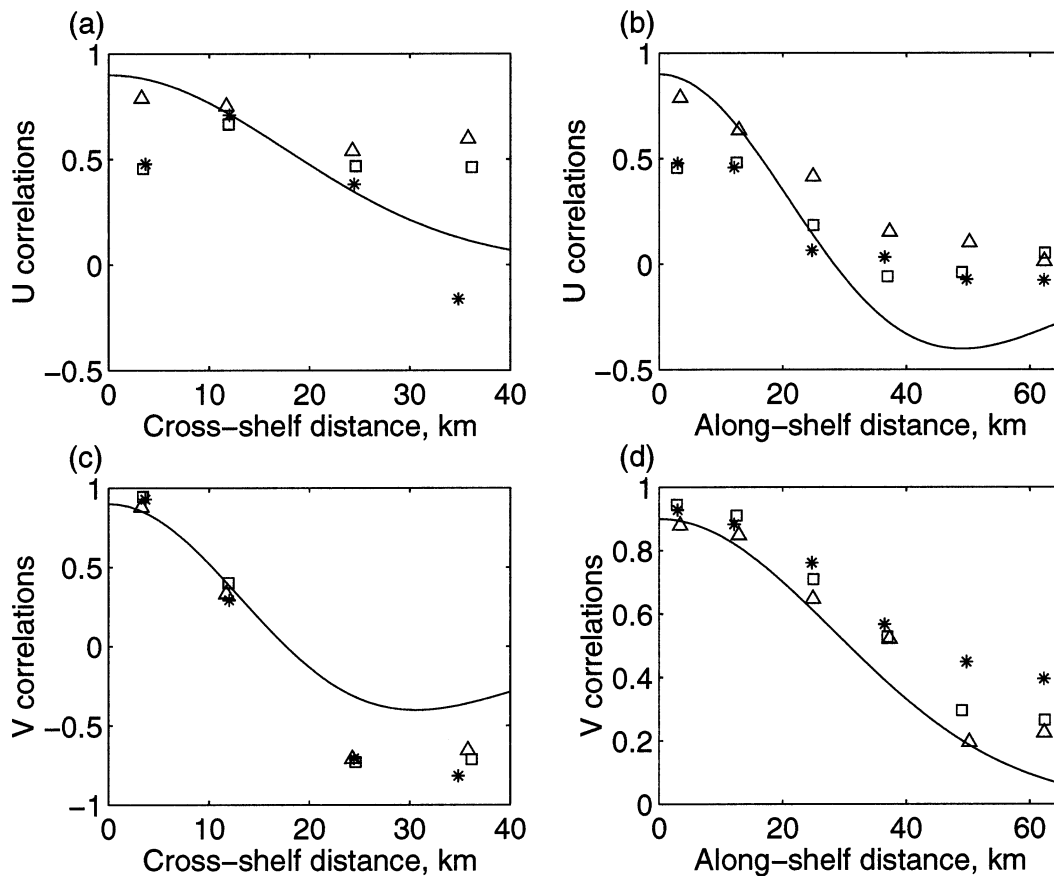


FIG. 5. Spatial correlations derived from the drifter data: (a) cross-shelf correlations of cross-shelf velocity (u), (b) along-shelf correlations of u , (c) cross-shelf correlations of along-shelf velocity (v), and (d) along-shelf correlations of v . The solid line indicates the correlations implied by the spatial structure specified in the text. The triangles, squares, and asterisks indicate the spatial correlations of the upwelling, surface convergent, and relaxation states, respectively.

where \mathbf{P} is the matrix of $\langle \psi, u \rangle$ and $\langle \psi, v \rangle$ between mapping and observation locations, \mathbf{Q} is the matrix of $\langle \chi, u \rangle$ and $\langle \chi, v \rangle$ between mapping and observation locations, \mathbf{A} is the matrix of $\langle u, u \rangle$, $\langle v, v \rangle$, and $\langle u, v \rangle$ and $\langle v, u \rangle$ between observation locations, ε is the fractional variance attributed to noise, \mathbf{I} is the identity matrix, and $\boldsymbol{\varphi}$ is the vector of u and v observations.

The employment of anisotropic structure functions is a very useful tool for OA over the shelf where the coastline imposes a condition of anisotropy. However, it is sometimes necessary to use isotropic structure functions over the shelf because of a lack of sufficient data to estimate different cross-shelf and along-shelf functions (Denman and Freeland 1985). Here there are sufficient drifter and moored data to estimate anisotropic spatial correlation functions in a curvilinear along-shelf and cross-shelf coordinate system. I choose a Gaussian correlation function of the form

$$F = \exp(-r^2/L_x^2 - s^2/L_y^2). \quad (8)$$

To determine the best estimates of ψ and χ , the noise level ε must be specified in addition to L_x and L_y . They

are chosen based on the observed spatial correlations of the bin-averaged along-shelf velocities for each state (Fig. 5). The along-shelf velocity correlations are used because they are better determined than those of the cross-shelf velocities. The cross-shelf velocities are weaker and subject to errors caused by small uncertainties in the cross-shelf direction. After subtracting the spatial mean along-shelf and cross-shelf velocities from each of the bin-averaged drifter velocities for each state, the correlations of along-shelf and cross-shelf pairs were determined within bins separated by 12.5 km. The bin correlations were then used to find L_x , L_y , and ε for the upwelling, surface convergence and relaxation states using a nonlinear least squares fit. In these least squares fits, ε was constrained to be at least 0.1. This was in recognition that even collocated independent velocity estimates are not perfectly correlated. This minimum fractional noise level is reasonable given that drifters are correlated with nearly collocated current meters at the 0.8 level. The drifter:current-meter correlations should be lower than drifter:drifter or current-meter:current-meter correlations because of different mea-

TABLE 2. Synoptic-state fractional errors and scales.

Synoptic state	ε	L_x (km)	L_y (km)
Upwelling	0.16	25.46	40.23
Surface convergent	0.10	24.15	43.21
Relaxation	0.10	23.07	57.98

surement technologies, measurement depths (1 vs 5 m), and small-scale spatial features. Moreover, processes such as Stokes drift affect drifters and current meters differently (Dever et al. 1998).

The least squares estimates of L_x , L_y , and ε are quite similar for the different states (Table 2). Based on these estimates, a common along-shelf decorrelation scale of 45 km, a cross-shelf scale of 25 km, and a noise level of 0.1 is used as shown in Fig. 5. These scales roughly match those of the moored array and are more than adequately resolved by the bin-averaged drifter data. They are capable of reproducing features such as the cyclone in the western Santa Barbara Channel but cannot reproduce smaller-scale features often seen in drifter trajectories such as flow through the interisland passes (Winant et al. 1999). The finding of longer decorrelation distances in the along-shelf direction is consistent with characteristics of shelf flow observed in numerous historical observational studies (e.g., Kundu and Allen 1976; Dever 1997).

The variance fraction of the velocity potential, v , is specified to be 0.15. This level is subjectively chosen based on the expectation that the divergent velocity is largely a function of the surface Ekman transport. Typical values of wind stress and surface mixed layer depth for this region imply Ekman transports on the order of 15% of the observed along-shelf velocities.

b. Synoptic average objective maps

The synoptic average objective maps are estimated from the drifter and current-meter data shown in Figs. 2–4 using the methodology outlined above. The mapping domain extends from the eastern Santa Barbara Channel to Estero Bay, from the easternmost current meter to the northernmost drifter deployment line. All maps presented are made using the correlation functions and fractional variance in the velocity potential specified in section 3b. As a sensitivity test, a variety of other mapping scales and specifications of velocity potential variance were examined. The mapped features described are not particularly sensitive to those changes.

1) UPWELLING

The upwelling streamfunction, velocity potential, and associated error maps are shown in Fig. 6. The streamfunction map (Fig. 6a) shows the steepest gradients are in the SMB, western SBC, and along the island coasts of the SBC. There is an equatorward flow, with some offshore tendency on the SMB. The streamlines between

Point Conception and Point Arguello form a boundary between flow that enters the SBC and continues out its eastern entrance and flow that heads south past the west side of San Miguel Island. The streamlines are aligned generally parallel to the coast except between Points Conception and Arguello where they are nearly perpendicular to the coast and east of Point Conception where several streamlines also intersect the coast. Velocities calculated from the streamfunction and velocity potential are also compared with the observed 5-m currents in Fig. 6a. There is generally good agreement. In several instances, the along-shelf component of flow is due to the streamfunction and the cross-shelf component is due to a combination of the streamfunction and velocity potential. In some cases, especially along the mainland SBC coast, the velocity potential acts to adjust the total estimated velocity vector to be more nearly parallel to the coast, in agreement with the observations.

The upwelling velocity potential map (Fig. 6b) shows the largest positive velocity potential is found in the western SBC with secondary maxima in the eastern SBC and over the midshelf of the SMB. Closed contours of the velocity potential indicate sources or sinks of flow, and the velocity estimates shown give a clear indication of a coherent source of surface currents in the western SBC.

The error maps for streamfunction (Fig. 6c) and velocity potential (Fig. 6d) show minimum error occur in the center of the mapping domain where abundant data exist. The error map for the streamfunction shows the greatest errors occur in the extreme north of the mapping region in the SMB. This is due to the relative lack of drifter observations in this area. The velocity potential map shows much greater errors than the streamfunction error map. This is caused by the low variance specified (0.15) in the velocity potential relative to the total.

2) SURFACE CONVERGENCE

The surface convergent streamfunction, velocity potential, and associated error maps are shown in Fig. 7. In contrast to the upwelling map, the steepest streamfunction gradients occur from the eastern SBC, continue along the mainland coast, and curve in a cyclonic direction in the western SBC. At Point Conception, the streamfunction indicates a jet that continues essentially westward past Point Arguello, becoming broader as it leaves the coast. In the SMB, streamfunction gradients are much weaker than for the upwelling case. They indicate weak southward flow that joins the westward jet at Point Arguello. In comparison with the upwelling case, streamfunction contours are aligned more nearly parallel to the coast. Currents from the velocity potential are also weaker, by about a factor of 2. The velocity potential serves much the same role as during the upwelling case, often helping to align the total estimated flow toward the observed flow by adjusting the cross-shelf component.

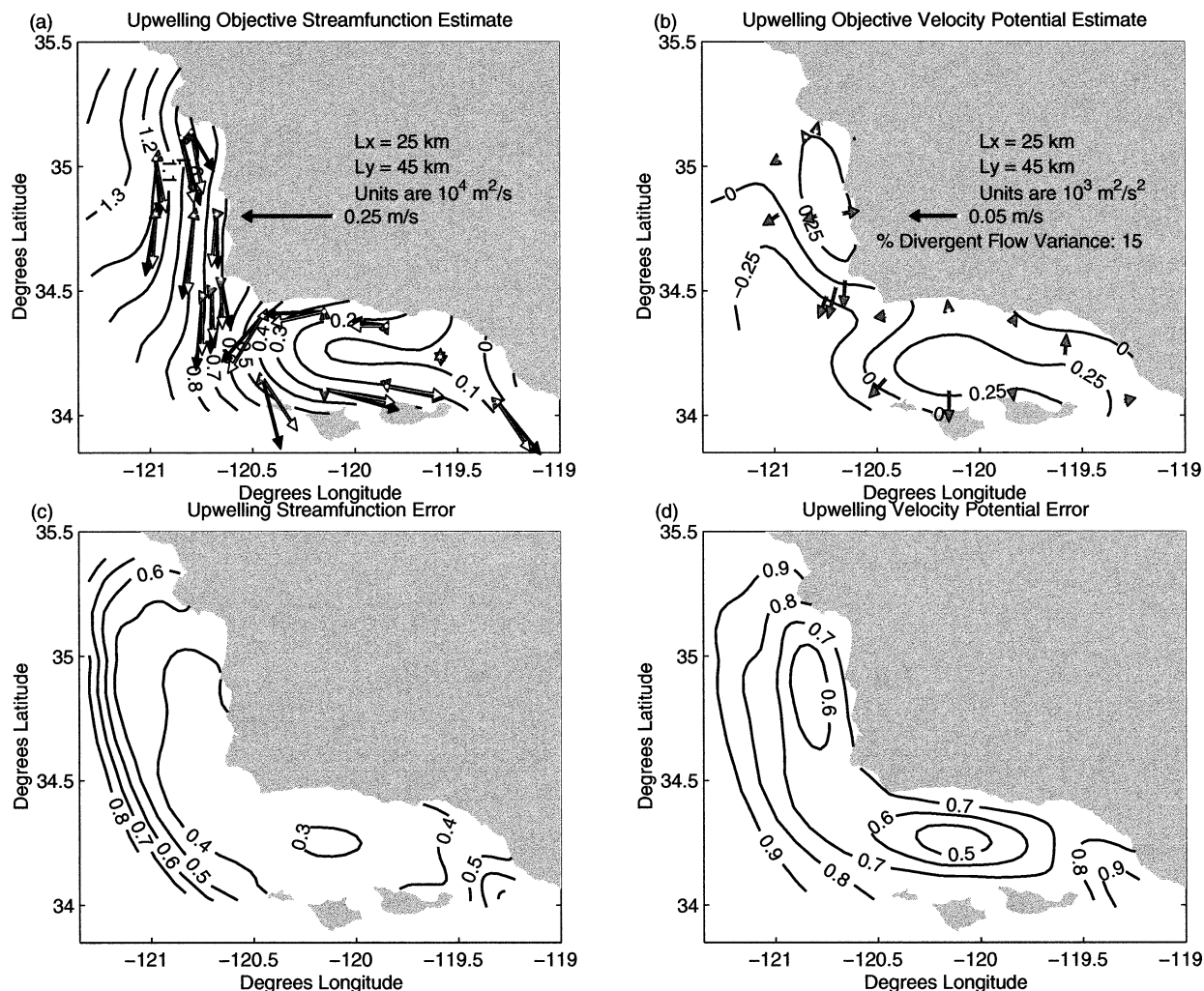


FIG. 6. Upwelling streamfunction, velocity potential, and error maps. (a) Observed 5-m currents are also indicated by the black arrows with the streamfunction surface current estimate indicated by the white arrows and the velocity potential current indicated by the gray arrows. (b) The velocity potential with velocities at the 5-m current meters indicated by the gray arrows. Note the scale change from (a). (c) The fractional error map for the streamfunction. (d) The fractional error map for the velocity potential.

The surface convergent velocity potential map (Fig. 7b) shows the largest positive velocity potential is found in the western SBC with a secondary maximum over the outer shelf of the SMB. Minima in the velocity potential occur over the broad shelf between Santa Barbara and Port Hueneme in the eastern SBC and in a region between Point Conception and Point Arguello. As with the upwelling case, the velocity estimates shown imply a source of surface currents in the western SBC.

The error maps for streamfunction (Fig. 7c) and velocity potential (Fig. 7d) again show minimum errors occur in the center of the mapping domain where abundant data surround the map grid points. The error map for the streamfunction shows the greatest errors occur in the extreme east of the SBC. This is due to the relative lack of drifter observations in this area. Despite the occurrence of relatively large errors here, the estimated

near-surface velocity agrees well with the observed velocity. The velocity potential map shows much greater errors than the streamfunction error map. The large error values in the eastern SBC indicate the negative velocity potential over the eastern SBC, and the velocities calculated from it should be treated with caution.

3) RELAXATION

The relaxation streamfunction, velocity potential, and associated error maps are shown in Fig. 8. The relaxation streamfunction resembles the surface convergent streamfunction in that the steepest streamfunction gradients occur from the eastern SBC and continue along the mainland coast. Although some streamfunction contours then curve in a cyclonic direction in the western SBC, most continue out past Point Arguello and northwest over the outer shelf of the SMB. The strongest

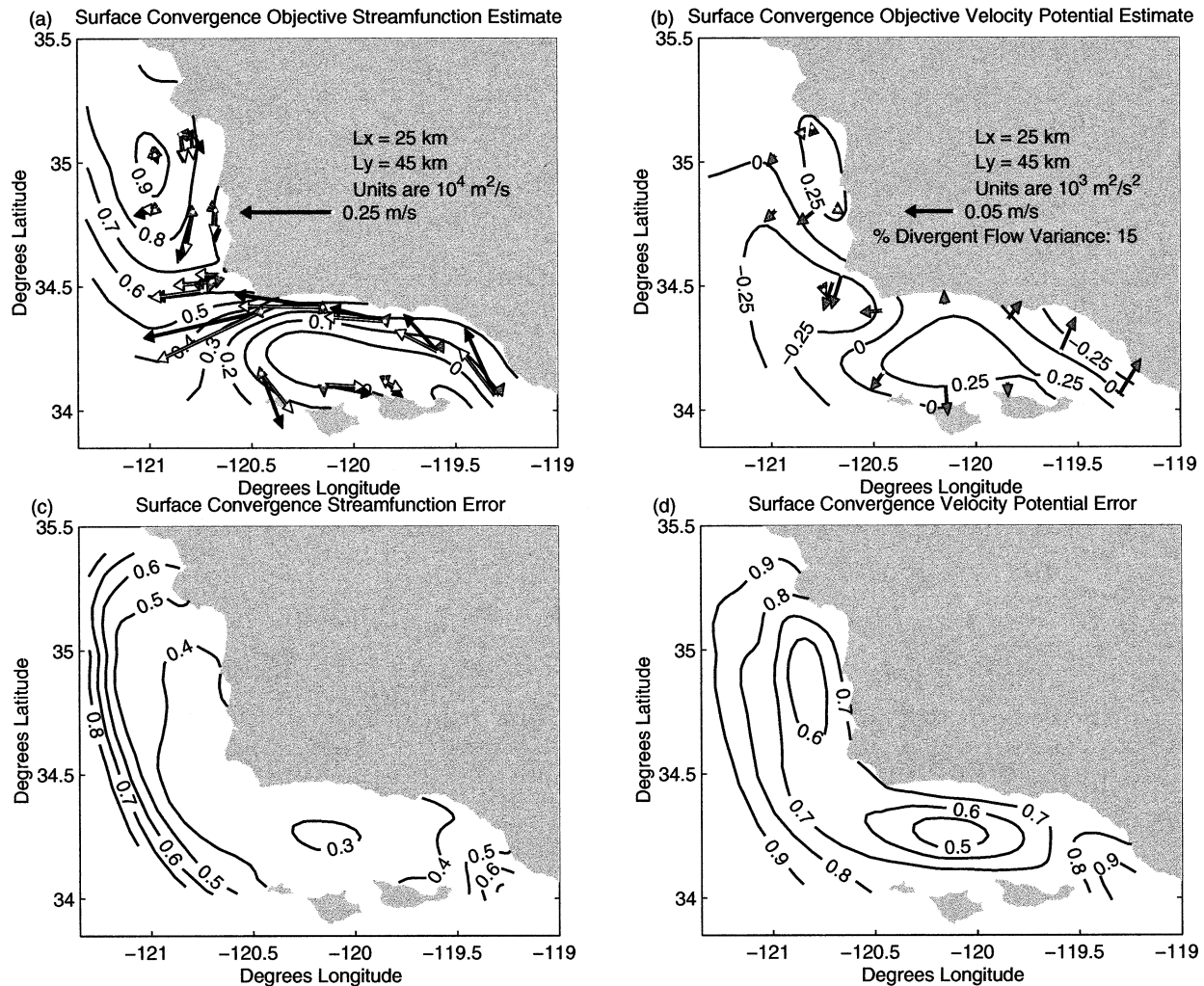


FIG. 7. (a) Surface convergent streamfunction (b) velocity potential, and (c), (d) error maps. See Fig. 6 for a complete explanation.

poleward flow in the SMB is found offshore with weaker flow occurring inshore of the 100-m isobath. As with the surface convergent case, streamfunction contours are aligned nearly parallel to the coast. Currents from the velocity potential are also weaker than the upwelling case. The velocity potential serves much the same role as during the upwelling case, often helping to align the total estimated flow toward the observed flow by adjusting the cross-shelf component.

The relaxation velocity potential map (Fig. 8b) shows the velocity potential maximum has moved westward relative to the upwelling and surface convergent cases. In contrast to the surface convergent case, there is little evidence of a minimum between Point Arguello and Point Conception.

The error maps Figs. 8c and 8d again show the greatest errors occur in the extreme east of the SBC where there is a lack of drifter observations. Comparison of Figs. 8d and 8b shows the relaxation velocity potential maximum has moved quite close to the edge of the

mapping region where errors increase and therefore should be interpreted cautiously.

4. Discussion

The surface streamfunction maps are well determined in the sense that they exceed the fractional noise. To test the sensitivity of the mapped fields to incremental changes in correlation scales, the streamfunction and velocity potential were mapped over scales ranging from 12.5 to 50 km in the cross-shelf direction and from 22.5 to 90 km in the along-shelf direction. Noise levels ranging from 5% to 50% were also considered. Spatial derivatives of the OA maps were also examined for this range of parameters. As long as the correlation scales exceeded the spatial resolution of the data, features in the OA maps were not overly sensitive to the choice of correlation scales. This is in concert with findings by Carter and Robinson (1987) and Denman and Freeland (1985). Although details changed, the features discussed

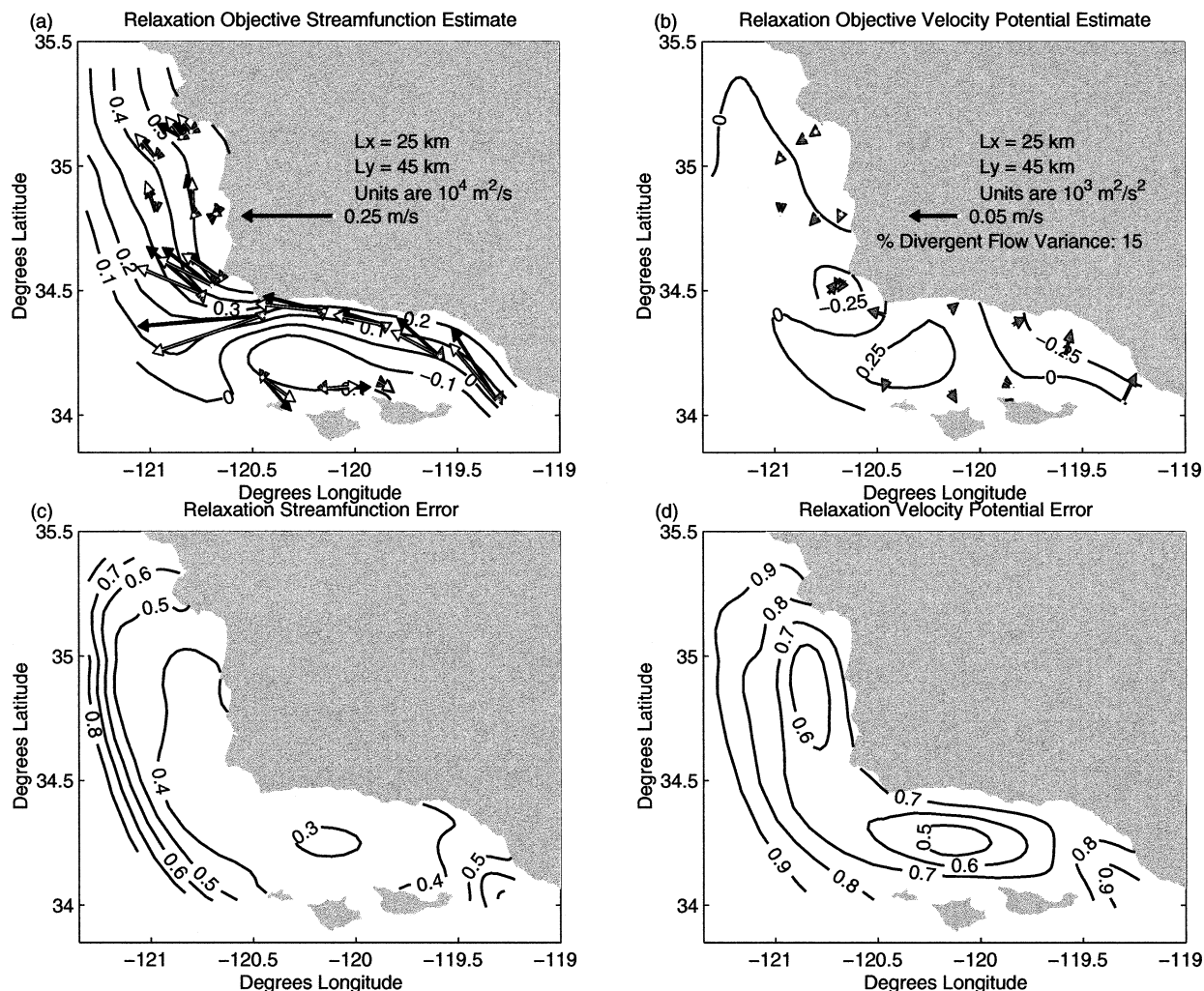


FIG. 8. (a) Relaxation streamfunction, (b) velocity potential, and (c), (d) error maps. See Fig. 6 for a complete explanation.

below are robust to changes in the correlation structure function that occur for different synoptic states or when considering different subdomains in the region (e.g., the Santa Maria Basin as opposed to the Santa Barbara Channel).

a. Vorticity

Figure 9 shows the estimated vorticity for the upwelling, surface convergence, and relaxation cases. It is scaled relative to the Coriolis parameter f and contoured only where the streamfunction error (Figs. 6c, 7c, 8c) is less than 0.5. For each state, there is a well-defined vorticity maximum in the western SBC. The cyclonic vorticity here is comparable to f , and it is strongest for the surface convergent state (greater than $0.4 f$). The vorticity magnitude is similar to that estimated by Münchow (2000) using lateral shear between current meters located at the north and south coasts of the western entrance to the SBC. Aside from this maximum, there

is a weak anticyclonic vorticity (0.1 – $0.2 f$) over the midshelf SMB for the upwelling and surface convergent states.

The magnitude of the vorticity maximum in the western SBC suggests the importance of nonlinear terms to the momentum balance. However, a calculation of the Coriolis terms relative to the advective terms shows the Coriolis terms to be far larger than the nonlinear terms in both the along-shelf and cross-shelf directions, suggesting the momentum balance in the western SBC is to first-order geostrophic. For the cross-channel momentum balance, the Coriolis terms are always more than an order of magnitude larger than the advective terms. For the along-channel momentum balance, the advective terms approach 20% of the Coriolis terms in the western channel.

The position of the cyclonic vorticity center in the western SBC varies for the different synoptic states. It is farthest east for the upwelling case and moves progressively west for the surface convergence and relax-

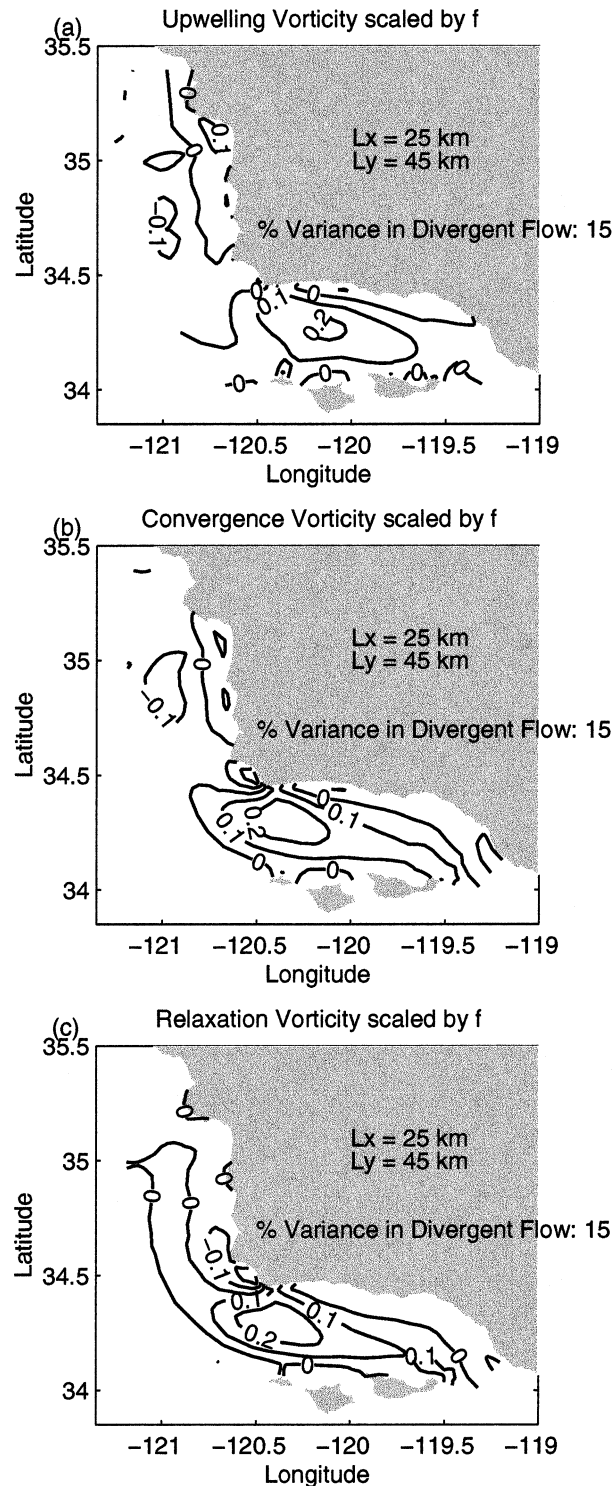


FIG. 9. Vorticity maps for (a) upwelling, (b) surface convergence, and (c) relaxation. Vorticity is scaled by the local Coriolis parameter f .

ation cases. It is always west of the center of the Santa Barbara Basin (Fig. 1) indicating that the cyclone is not trapped to the bottom bathymetry.

A number of ideas have been advanced to explain the western cyclone in the Santa Barbara Channel. These include viscous production and advection of vorticity from the SMB into the SBC (Oey 1996), divergence in the western channel caused by local wind stress curl (Münchow 2000; Wang 1997; Chen and Wang 2000), and the generation of a poleward pressure gradient by southern California Bight scale wind stress curl (Wang 1997; Oey 1999; Chen and Wang 2000).

Of these three mechanisms, Figs. 6–9 support the advection of vorticity least. For two of the three states (surface convergence and relaxation), flow is poleward (westward) at Point Conception, and advection of vorticity into the channel cannot occur. Moreover, the observed vorticity over much of the SMB is anticyclonic, as contrasted with the cyclonic vorticity in the western channel.

Previous studies suggest both local wind stress curl and a poleward pressure gradient may be important to the development of the cyclonic vorticity maximum in the western channel. Münchow (2000) found a significant correlation between the wind stress (which was a proxy for wind stress curl) and the cyclonic shear observed at the western entrance to the channel for data acquired between January and July 1984. Wang (1997) showed how a simple model with wind stress curl could generate a cyclonic circulation as could the same model when driven with a poleward pressure gradient. However, a more sophisticated later model (Chen and Wang 2000), driven with a realistic spatially varying wind field generated poleward flow along the mainland SBC coast but did not generate a strong cyclonic circulation. Rather, the assimilation of observed temperature data into the model accounted for the cyclonic circulation. Chen and Wang explained the improved performance of the temperature assimilating case by its implicit inclusion of a poleward pressure gradient.

b. Wind stress curl

The method described in section 3 can be used to describe the wind stress and wind stress curl present during different synoptic states by mapping moored and shore station wind measurements (Fig. 1). Data at coastal and buoy meteorological stations active over the same period as the mooring and drifter program are used. To facilitate comparisons with the velocity data, the wind data are mapped on the same spatial scales. However, the wind data are mapped using the streamfunction alone; that is, horizontal nondivergence is imposed. Wind stress is estimated using the Large and Pond (1981) neutral stability bulk coefficients, and wind stress streamfunctions are mapped directly from the wind stress estimates.

The resulting wind stress streamfunctions and curl

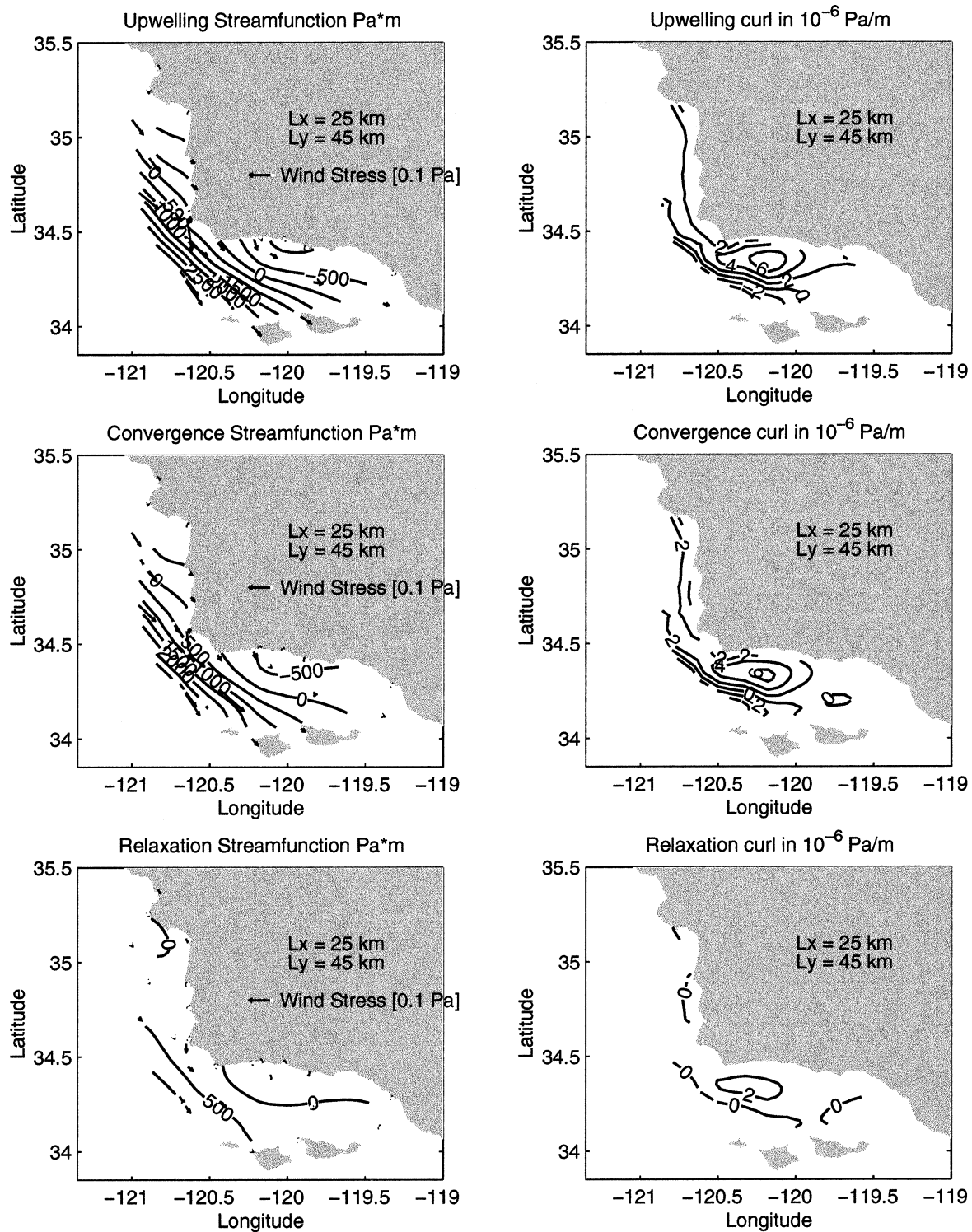


FIG. 10. Average winds and wind stress curl during upwelling, surface convergent, and relaxation conditions. The streamfunction is estimated using the same length scales as those used for the surface currents. The curl is calculated in the area within the perimeter of the measurements and where the fractional error is less than 0.5. A wind stress curl of 10^{-6} Pa m^{-1} corresponds to an upwelling rate of approximately 1 m day^{-1} .

patterns are presented in Fig. 10. The wind stress and wind stress curl for the upwelling and surface convergence states are nearly identical (Figs. 10a,b). The wind stress occurring during relaxation events (Fig. 10c) is much smaller. This is consistent with Harms and Winant (1998) who found that strong wind stress could result in either upwelling or cyclonic circulation, depending on the strength of the along-shelf pressure gradient, and relaxation occurred during weak wind events. The fact that strong cyclonic circulation remains during weak winds is evidence that wind stress curl is not the only factor driving cyclonic circulation in the western SBC. This is consistent with the modeling results of Chen and Wang (2000).

The upwelling rates implied by the wind stress curl are up to 6 m day^{-1} in the western channel for the upwelling and convergence states. The maximum wind stress curl occurs south of Point Conception between the mainland coast and mid channel. The maxima found here compare reasonably well with those found by Münchow (2000) using aircraft data during specific events. Averaging over 20 aircraft flights from the spring of 1983, he found a mean maximum rate of 4 m day^{-1} in the western channel with rates of up to 20 m day^{-1} occurring on some flights.

c. Divergence

The surface velocity potential (Figs. 6b, 7b, 8b) indicates a velocity source in the western Santa Barbara Channel. This source is nearly collocated with the cyclonic vorticity maximum and is close to the wind stress curl maxima (Fig. 10). Ideally one could use the velocity potential to calculate near-surface divergence and compare it quantitatively with the Ekman transport divergence. Unfortunately, the surface velocity potential is much weaker, noisier, and more subject to errors than the velocity or wind streamfunctions. This makes direct estimates of divergence from the velocity potential problematic (Fig. 11). Upwelling rates implied by the surface divergence are similar in magnitude to those implied by the wind stress curl (Fig. 10). However, the close alignment of divergence contours with the along-shelf boundaries of the mapping domain indicates the calculated divergence is heavily influenced by values along these boundaries where the error is largest. For this reason, the divergence estimates from the velocity potential are almost certainly inaccurate.

d. Mapping limitations

The procedures for conditionally averaging drifter observations by synoptic state and mapping velocity data in a coastline following coordinate system were developed to maximize the spatial resolution provided by observations and to be consistent with available information about the observed kinematics. However, important limitations on the results exist.

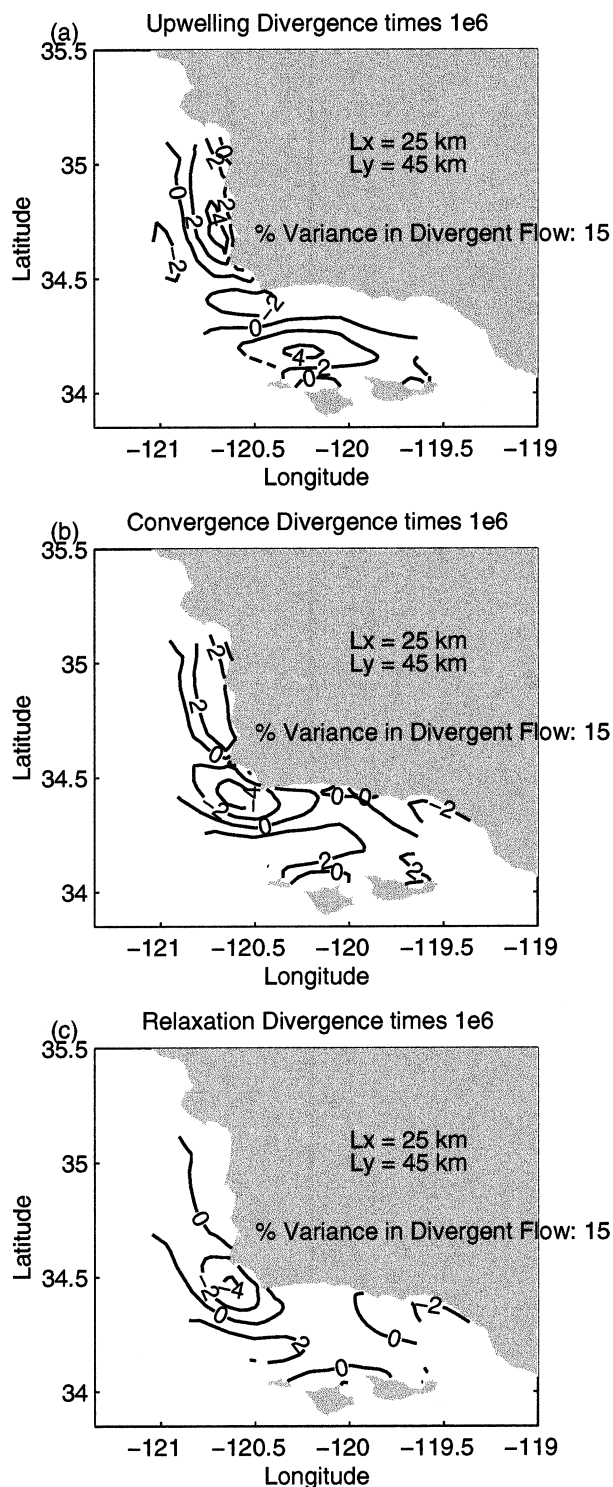


FIG. 11. Surface divergence maps for (a) upwelling, (b) surface convergence, and (c) relaxation. It is contoured only where the velocity potential error (Figs. 6d, 7d, and 8d) is less than 0.5. Units are 10^{-6} s^{-1} . For a 25-m-thick surface layer, this corresponds to vertical velocities of about 2 m day^{-1} .

One major limitation is the categorization of a constantly evolving flow field in terms of three static states. The events that make up the composite states are smeared out in these average states. For example, the time-varying flow fields show that the cyclonic recirculation in the western SBC is not simply a forced feature of the flow. Cyclonic features generated in the SBC can propagate westward at a speed of 0.06 m s^{-1} from Santa Rosa Island to the western entrance to the channel (Harms and Winant 1998). These features may have characteristics of hybrid Rossby and Kelvin waves (Beckenbach and Washburn 2002). Similarly, the westward jet at Point Conception seen in the surface convergent flow (Fig. 7a) is stronger and does not become more diffuse away from the shelf but rather takes a variety of paths as seen in hydrographic observations (e.g., Atkinson et al. 1986). Conclusions about the forcing mechanisms and importance of nonlinear terms do not take into account the time history of forcing required to produce the synoptic states. For example, the western cyclone is predominantly geostrophic, but this does not mean that nonlinear terms were not important in its generation.

Another limitation results from mapping the flow using constant scales in the along-shelf (45 km) and cross-shelf (25 km) directions. Features smaller than these scales will be blurred or will not show up at all. One such feature is the adjustment of Ekman transport to the coastal boundary condition of no flow through the coast. This provides the classical mechanism for coastal upwelling. It occurs when the total water depth decreases to the Ekman depth (Clarke and Van Gorder 1986). In practice this is about 50 m. For the Santa Barbara Channel and Santa Maria Basin, these depths are within 3–5 km of the coast. An indication of the necessity to adjust to the coastal boundary condition is shown in the streamfunction maps that often imply some flow into or out of the coast, especially in the regions between Point Arguello and Point Conception and along the mainland coast immediately east of Point Conception. One reasonable interpretation of these features is that they are the expression of coastal upwelling and that the adjustment to no flow through the coast occurs on scales finer than are possible to map using the existing data. Although not the focus of this paper, the limitations on mapping scales may be more severe for the wind maps (Fig. 10). Aircraft overflights (e.g., Münchow 2000) show sharp discontinuities in the wind field south of Point Conception for upwelling-favorable winds.

5. Conclusions

The flow field near Point Conception is spatially complex. Although the drifter database provides adequate spatial resolution of the flow fields, it is biased in that it undersamples upwelling conditions. This makes simple seasonal or overall means inaccurate. To remedy this, drifter velocities were classified in terms of three

large-scale synoptic states (upwelling, surface convergence, and relaxation) developed for the Santa Barbara Channel–Santa Maria Basin region. The states were defined using long-term current-meter moorings at the eastern and western entrances to the channel and in the Santa Maria Basin. When averaged by synoptic state, the drifters agree well with the current meters. Spatial correlations of drifter averages show along-shelf scales are approximately 45 km and cross-shelf scales are approximately 25 km for all three synoptic states.

The spatial resolution provided by the drifter velocities makes it possible to map synoptic flow fields using objective analysis. A streamfunction and velocity potential representation is used, and the fields are mapped in a curvilinear coordinate system that follows the coast. The fractional variance in the velocity potential (0.15) was chosen based on estimates of the Ekman transport relative to the along-shelf transport. The fractional variance in the error (0.1) was chosen based on the correlation of drifters with nearby current meters. The results presented use the spatial scales based on the observations, but a variety of other scales and variance in the velocity potential were tested.

The synoptic-state streamfunctions are well determined and are not particularly sensitive to the exact correlation scales chosen. Streamlines generally follow the coastline, except near Point Conception and Point Arguello, where they intersect the coast for the upwelling and surface convergence states. This is likely to be an indication of coastal upwelling. The streamfunctions allow the calculation of vorticity maps for the three states. The dominant feature of all three of these maps is a cyclonic vorticity center in the western Santa Barbara Channel. Its magnitude is similar for the three flow states. The vorticity maximum shifts progressively westward from the upwelling to the relaxation state. The shift in position of the cyclone for different states argues it is not tied to the bathymetry. Although the vorticity maximum is a significant fraction of the Coriolis parameter ($0.3\text{--}0.4f$), the momentum balance indicates the Coriolis terms outweigh nonlinear and wind stress terms in the along-shelf and cross-shelf directions. This indicates the momentum balance is predominantly geostrophic for the three states discussed here.

Using available wind time series, the wind stress can be mapped on the same scales as the velocity. The wind maps show strong wind stress curl in western channel for the upwelling and surface convergent states. The wind and wind stress curl are much weaker for the relaxation state. The fact that the cyclone remains during weak wind forcing argues that it is not simply forced by wind stress curl.

The velocity potential is much weaker than the streamfunction. Along the coast, the velocity from the velocity potential helps to align the mapped flow with the coastline. In the western channel, it provides a broad indication of a velocity source. This source is nearly collocated with the cyclone in the western channel.

However, the noisiness of the velocity potential means that it cannot be used to make quantitative divergence estimates.

In this work, I have tried to push the kinematic analysis of velocity data as far as possible. The drifter data were used to provide spatial resolution, and the moored data were used to average the drifter observations in a way that accounted for their large-scale bias. Velocity averages were then mapped in a coastline-following coordinate system on observed spatial scales. Realistic values for the fractional variance in the divergent flow and noise were chosen. The results for the streamfunction are quite good. They are not overly sensitive to small changes in the mapping scales or velocity potential variance, and reasonable calculations of vorticity can be made from them.

However, the velocity potentials remain noisy, and quantitative estimates of divergence cannot be made from them. The understanding of near-surface divergence is crucial to the general understanding of upwelling and its consequences on the coastal ecosystem response. The near-surface velocity and wind observations in the Point Conception region are about the best one can practically make, and the wind stress curl and expected near-surface divergence are exceptionally strong here. The inability of even a careful kinematic mapping procedure to make good divergence estimates argues that further advances must come from the coupling of submesoscale atmospheric (e.g., Koracin and Dorman 2001) models to oceanic models that include data assimilation (e.g., Oke et al. 2002).

Acknowledgments. Support for this work was provided by Cooperative Agreement 14-35-0001-30571 between the Minerals Management Service and the Scripps Institution of Oceanography (SIO) at the University of California, San Diego. Dong-Ping Wang (State University of New York) suggested using the moorings to objectively map the near-surface flow field. Clint Winant and Myrl Hendershott (SIO) provided useful feedback and suggestions for improvement of this manuscript. Clive Dorman (SIO) has been a tireless advocate for acquiring wind measurements sufficient to map the spatial structure of wind forcing and to test its importance. A great number of people are to be thanked for the success of the drifter and moored programs—foremost among these are Douglas Alden and Paul Harvey (SIO).

REFERENCES

- Atkinson, L. P., K. H. Brink, R. E. Davis, B. H. Jones, T. Paluskiewicz, and D. W. Stuart, 1986: Mesoscale hydrographic variability in the vicinity of Point Conception and Arguello during April–May 1983: The OPUS 1983 experiment. *J. Geophys. Res.*, **91**, 12 899–12 918.
- Auad, G., and M. C. Hendershott, 1997: The low frequency transport in the Santa Barbara Channel: Description and forcing. *Cont. Shelf Res.*, **17**, 779–802.
- Barth, J. A., and K. H. Brink, 1987: Shipboard acoustic Doppler profiler velocity observations near Point Conception: Spring 1983. *J. Geophys. Res.*, **92**, 3925–3943.
- Beckenbach, E., and L. Washburn, 2002: Observations of wavelike phenomena in the Santa Barbara Channel using HF radar. *Eos, Trans. Amer. Geophys. Union*, **83** (Suppl. 3), Abstract OS32D-160.
- Bray, N. A., A. Keyes, and W. M. L. Morawitz, 1999: The California Current System in the Southern California Bight and the Santa Barbara Channel. *J. Geophys. Res.*, **104**, 7695–7714.
- Brink, K. H., and R. D. Muench, 1986: Circulation in the Point Conception–Santa Barbara Channel region. *J. Geophys. Res.*, **91**, 877–895.
- Carter, E. F., and A. R. Robinson, 1987: Analysis models for the estimation of ocean fields. *J. Atmos. Oceanic Technol.*, **4**, 49–74.
- Chen, C.-S., and D.-P. Wang, 2000: Data assimilation model study of wind effects in the Santa Barbara Channel. *J. Geophys. Res.*, **105**, 22 003–22 014.
- Clarke, A. J., and S. Van Gorder, 1986: A method for estimating wind-driven frictional, time-dependent, stratified shelf and slope water flow. *J. Phys. Oceanogr.*, **16**, 1013–1028.
- Daley, R., 1985: The analysis of synoptic scale divergence by a statistical interpolation procedure. *Mon. Wea. Rev.*, **113**, 1066–1079.
- Davis, R. E., 1985: Drifter observations of coastal surface currents during CODE: The method and descriptive view. *J. Geophys. Res.*, **90**, 4741–4755.
- , 1991: Observing the general circulation with floats. *Deep-Sea Res.*, **38**, S531–S571.
- Denman, K. L., and H. J. Freeland, 1985: Correlation scales, objective mapping and a statistical test of geostrophy over the continental shelf. *J. Mar. Res.*, **43**, 517–539.
- Dever, E. P., 1997: Subtidal velocity correlation scales on the northern California shelf. *J. Geophys. Res.*, **102**, 8555–8571.
- , and C. D. Winant, 2002: The evolution and depth structure of shelf and slope temperatures and velocities during the 1997–1998 El Niño near Point Conception, California. *Progress in Oceanography*, Vol. 54, Pergamon, 77–103.
- , M. C. Hendershott, and C. D. Winant, 1998: Statistical aspects of surface drifter observations of circulation in the Santa Barbara Channel. *J. Geophys. Res.*, **103**, 24 781–24 797.
- Dorman, C. E., and C. D. Winant, 2000: The structure and variability of the marine atmosphere around the Santa Barbara Channel. *Mon. Wea. Rev.*, **128**, 261–281.
- Gille, S. T., 2003: Float observations of the Southern Ocean. Part I: Estimating mean fields, bottom velocities, and topographic steering. *J. Phys. Oceanogr.*, **33**, 1167–1181.
- Harms, S., and C. D. Winant, 1998: Characteristic patterns of the circulation in the Santa Barbara Channel. *J. Geophys. Res.*, **103**, 3041–3065.
- Hendershott, M. C., 2000: Observations of circulation in the Santa Maria Basin. Center for Coastal Studies Quality Review Board minutes, Meeting 7, Scripps Institution of Oceanography, University of California, San Diego, La Jolla, CA, 419 pp.
- , and C. D. Winant, 1996: Surface circulation in the Santa Barbara Channel. *Oceanography*, **9**, 114–121.
- Koracin, D., and C. E. Dorman, 2001: Marine atmospheric boundary layer divergence and clouds along California in June 1996. *Mon. Wea. Rev.*, **129**, 2040–2056.
- Kundu, P. K., and J. S. Allen, 1976: Some three-dimensional characteristics of low-frequency current fluctuations near the Oregon coast. *J. Phys. Oceanogr.*, **6**, 181–199.
- Large, W. G., and S. Pond, 1981: Open ocean momentum flux measurements in moderate to strong winds. *J. Phys. Oceanogr.*, **11**, 324–336.
- McCreary, J. P., P. K. Kundu, and S.-Y. Chao, 1987: On the dynamics of the California Current System. *J. Mar. Res.*, **45**, 1–32.
- Morse, P. M., and H. Feshbach, 1953: *Methods of Theoretical Physics, Part I*. McGraw-Hill, 997 pp.

- Münchow, A., 2000: Wind stress curl forcing of the coastal ocean near Point Conception, California. *J. Phys. Oceanogr.*, **30**, 1265–1280.
- Oey, L.-Y., 1996: Flow around a coastal bend: A model of the Santa Barbara Channel eddy. *J. Geophys. Res.*, **101**, 16 667–16 682.
- , 1999: A forcing mechanism for the poleward flow off the southern California coast. *J. Geophys. Res.*, **104**, 13 529–13 539.
- Oke, P. R., J. S. Allen, R. N. Miller, and G. D. Egbert, 2002: A modeling study of the three-dimensional continental shelf off Oregon. Part II: Dynamical analysis. *J. Phys. Oceanogr.*, **32**, 1383–1403.
- Pedder, M. A., 1989: Limited area kinematic analysis by a multivariate statistical interpolation method. *Mon. Wea. Rev.*, **117**, 1695–1708.
- Rogerson, A. M., 1999: Transcritical flows in the coastal marine atmospheric boundary layer. *J. Atmos. Sci.*, **56**, 2761–2779.
- Strub, P. T., J. S. Allen, A. Huyer, R. L. Smith, and R. C. Beardsley, 1987: Seasonal cycles of currents, temperatures, winds and sea level over the northeast Pacific continental shelf: 35N to 48N. *J. Geophys. Res.*, **92**, 1507–1526.
- Swenson, M. S., and P. P. Niiler, 1996: Statistical analysis of the surface circulation of the California Current. *J. Geophys. Res.*, **101**, 22 631–22 645.
- Wang, D.-P., 1997: Effects of small-scale wind on coastal upwelling with application to Point Conception. *J. Geophys. Res.*, **102**, 15 555–15 566.
- Winant, C. D., D. J. Alden, E. P. Dever, K. A. Edwards, and M. C. Hendershott, 1999: Near-surface drifter trajectories off central and southern California. *J. Geophys. Res.*, **104**, 15 713–15 726.
- , E. P. Dever, and M. C. Hendershott, 2003: Characteristic patterns of shelf circulation at the boundary between central and southern California. *J. Geophys. Res.*, **108**, 3021, doi:10.1029/2001JC001302.